



**Accelerated discovery and mechanical property
characterization of bioresorbable amorphous alloys in the
Mg-Zn-Ca and the Fe-Mg-Zn systems using high-throughput
methods.**

Journal:	<i>Journal of Materials Chemistry B</i>
Manuscript ID	TB-ART-06-2019-001302.R1
Article Type:	Paper
Date Submitted by the Author:	18-Jul-2019
Complete List of Authors:	Datye, Amit; Yale University, Department of Mechanical Engineering and Materials Science Kube, Sebastian; Yale University, Department of Mechanical Engineering and Materials Science Verma, Devendra; Nanoscience Instruments Schroers, Jan; Yale University, Department of Mechanical Engineering and Materials Science Schwarz, Udo; Yale University, Department of Mechanical Engineering and Materials Science; Yale University, Department of Chemical Engineering

**Accelerated discovery and mechanical property characterization of
bioresorbable amorphous alloys in the Mg-Zn-Ca and the Fe-Mg-Zn systems
using high-throughput methods.**

Amit Datye^{1,*}, Sebastian A. Kube¹, Devendra Verma³, Jan Schroers¹, and Udo D. Schwarz^{1,2,*}

¹ Department of Mechanical Engineering and Materials Science, Yale University, New Haven, CT 06511, USA.

² Department of Chemical Engineering, Yale University, New Haven, CT 06511, USA.

³ Nanoscience Instruments, 10008 S. 51st Street, Ste 110. Phoenix, AZ 85044 USA.

* Corresponding authors. E-mails: amit.datye@yale.edu; udo.schwarz@yale.edu

ABSTRACT

Ternary amorphous alloys in the magnesium (Mg)- zinc (Zn)- calcium (Ca) and the iron (Fe)- Mg-Zn systems are promising candidates for use in bioresorbable implants and devices. The optimal alloy compositions for biomedical applications should be chosen from a large variety of available alloys with best combination of mechanical properties (modulus, strength, hardness) and biological response (in-situ degradation rates, cell adhesion and proliferation). As a first step towards establishing a database designed to enable such targeted material selection, amorphous alloy composition libraries were fabricated employing a combinatorial magnetron sputtering approach where Mg, Zn, and Ca/Fe are co-deposited from separate sources onto a silicon wafer substrate. Composition analysis using energy dispersive X-ray spectroscopy documented a composition range of ~15 – 85 at. % Mg, ~6 – 55 at. % Zn, and ~5 - 60 at. % Ca for the Mg-Zn-Ca library and ~26 – 84 at. % Mg, ~10 – 61 at. % Zn, and ~7 - 55 at. % Fe for the Fe-Mg-Zn library. X-ray diffraction measurements established that amorphous alloys (i.e., glasses) form in almost the entire range of composition at the high cooling rates during sputtering for both alloy libraries. Finally, the effective material modulus, the Oliver-Pharr hardness, and the yield strength values obtained using nanoindentation reveal a wide range of mechanical properties within both systems.

KEYWORDS

bioresorbable alloys, bulk metallic glass, nanoindentation, yield strength.

1. INTRODUCTION

Magnesium (Mg), zinc (Zn), calcium (Ca) and iron (Fe) based alloys have attracted considerable attention in recent years as bioresorbable materials for implant and coating applications due to their ability to provide necessary mechanical support for the tissue reconstruction process and resorb into the body over time without being toxic. For example, Mg is an activator of many enzymes, coregulator of protein synthesis and muscle contraction, supports neurological and digestive function, promotes growth of human bones, and is a stabilizer of DNA and RNA^{1, 2}. Like Mg, Zn is a very important element for proper functions of human body. In trace amounts it supports the immune system and the synthesis of enzymes, proteins etc.³. The biocompatibility of pure Mg and pure Zn in general both in vitro tests with cell cultures and in vivo tests with animals is very good^{3, 4}. Magnesium alloys also have low density ($\sim 2.0 \text{ gm.cm}^{-3}$) and low elastic modulus (25 - 45 GPa)^{5, 6}, which is closer to that of the human bones (10 - 40 GPa)⁷ in comparison with other metallic biomaterials.

Despite this potential, currently available Mg- or Zn-based alloys feature several drawbacks with respect to their suitability for clinical applications. Microgalvanic corrosion⁸⁻¹¹, e.g., is observed in crystalline Mg alloys due to the electrochemical potential differences between the secondary phase and the magnesium matrix¹², which causes the Mg alloys to have a faster corrosion rate than desired and results in a rapid loss of mechanical strength along with evolution of hydrogen at a rate faster than can be dissolved in the surrounding tissue¹³. Detachment of the secondary phase in the form of particulates due to localized corrosion has also been previously documented¹⁴. In addition, research by Gu et al.² on the biocompatibility and mechanical and corrosion properties of cast Mg alloys with 1 wt.% of nine different alloy elements revealed that adding Al, Zn, or Zr improved the strength and the corrosion resistance compared to pure Mg

while the addition of Si and Y had negative effect on corrosion properties ². Finally, studies on bioresorbable Mg alloys for stents ^{4,15}, which focused on degradation rates, biocompatibility, and the effect of the alloys on vascular endothelial cells and smooth muscle cells, showed that the excessive degradation rate of Mg alloys also restricts its large-scale clinical application.

Moving forward, the question arises how to discover and fabricate alloys that are non-toxic but otherwise feature all characteristics required for use in implants or coatings, such as the mechanical properties needed to support the forces acting on them combined with their ability to fully resorb after the body has healed enough to support these forces on its own. Ideally, one should be able to choose the material from a database to match the exact specifications needed to optimize their intended performance. Towards this goal, one strategy to minimize excessive degradation rates and other negative effects in bioresorbable alloys is microstructure engineering of these alloys, such as grain boundary refinement or adding additional phases. As an alternative approach, several other studies have used the addition of alloying elements like Ca and rare earth metals elements to Mg- and Zn-based alloys ¹⁶ to create bi- and poly-phase alloys with improvements in mechanical properties and reducing degradation rates. However, although generally these alloys progressively degrade with no allergic reactions, their long-term clinical results are still not completely clear. Alloying materials and concentration must therefore be carefully selected keeping mechanical strength, cytotoxicity, and hemocompatibility into consideration.

In this work, amorphous metallic alloys (glass) are used instead of crystalline metallic alloys. Since Mg- and Zn-based alloys represent the only group of materials that have already been applied in pre-clinical tests with human patients, this research focuses on the Mg-Zn-Ca and Fe-Mg-Zn alloy systems. To establish an ability to rapidly screen a large number of different alloy compositions, we utilize a high-throughput approach for alloy creation, structural analysis, and

mechanical property testing. Combining the data then allows to identify trends in the complex interplay of composition, structure, and mechanical properties.

Background

To be able to produce implants of adequate size, candidate materials need to feature dimensions of at least several centimeters. When an amorphous metal-based alloy (i.e., a ‘metallic glass’) satisfies this requirement, it is referred to as *bulk metallic glass* (BMG). Compared to their crystalline counterparts, BMGs typically exhibit higher strength, good fatigue endurance, and excellent wear and corrosion resistance, but also lower Young’s moduli^{17,18}. Furthermore, BMGs can be readily patterned, and such patterns can be used to functionalize the material by, e.g., programming a desirable cellular response through imprinting specific nanopatterns at the implant’s surface¹⁹⁻²². A number of different BMG compositions, such as platinum-, zirconium-, iron-, or magnesium-based alloys, have already been evaluated for their biocompatibility and biodegradability²³⁻²⁵, and some show great potential as biomaterials for hard tissue, devices, and sensors. However, these previously studied alloys have not been optimized or specifically selected for specific biomedical applications considering mechanical compliance with the host tissue.

More generally, bioresorbable BMGs based on the elements Mg, Zn, Ca, and Fe have great potential as bone implants or fillers, cardiovascular implants, sutures, and dental fillers due to their attractive mechanical and electrochemical properties. In 2005, Gu et al.²⁶ reported the first Mg-Zn-Ca-based BMGs, and since then Mg-based BMGs have been widely studied for bioresorbable implant and coating applications. Senkov et al.²⁷ studied a range of compositions in the Mg-Zn-Ca system and concluded that the glass forming ability for these alloys is very sensitive to compositional changes. Zberg et al.²⁸ did a comparative study of Mg-Zn-Ca crystalline and amorphous (BMG) alloys in-vitro and in-vivo and found that while the strength and the elastic

limit of the BMGs was orders higher, it was lower in plasticity, which is not ideal for vascular applications like stents. They concluded that Zn is the key for reducing the hydrogen evolution in Mg and increasing the tissue healing; as a consequence, Zn-rich $\text{Mg}_{60+x}\text{Zn}_{35-x}\text{Ca}_5$ ($0 \leq x \leq 7$) glasses may represent ideal candidates for bioresorbable implant applications. Ramya et al.²⁹ studied partially amorphous and fully crystalline samples of both $\text{Mg}_{66}\text{Zn}_{30}\text{Ca}_4$ and $\text{Mg}_{60}\text{Zn}_{35}\text{Ca}_5$ glasses. Their research provided two important conclusions: First, the corrosion resistance doubled with a 5% increase in Zn, and second, the corrosion rate of amorphous samples was two orders less than their crystalline counterparts.

In contrast, few researchers have studied Zn-based BMGs as bioresorbable implant materials. Jiao et al.³⁰ studied Zn-based BMGs with different compositions and found that the composition of $\text{Zn}_{40}\text{Mg}_{11}\text{Ca}_{31}\text{Yb}_{18}$ with properties comparable to that of a human bone along with a low glass transition temperature is suitable for thermoplastic processing. In a review of Mg-based, Fe-based, and Zn-based bioresorbable metallic alloys, Li et al.³¹ concluded that while Mg-based alloys have had clinical trials, Zn-based alloys hold the most promise. Other researchers found that the corrosion potential decreases for lower Ca-content glasses³² and that an increase in the Zn concentration improves the glass forming ability of the alloy³³. Table 1 lists the mechanical properties of a few of the Mg-Zn-Ca BMG compositions as reported by previous studies. Preliminary examination on the Mg-Zn-Ca³⁴ alloy system with 12 different elemental compositions ranging from 35.9–63 at.% for Mg, 4.1–21 at.% for Ca, and 17.9–58.3 at.% for Zn complementary to these mechanical characterizations has shown that while there is a clear relationship between Zn content and the corrosion rate of the Mg-Zn-Ca BMG, a higher Zn content was also observed to have poor cell viability.

But even though the Mg-Zn-Ca metallic glass system has been studied for biomedical applications and has been of great interest within the last decade, the optimal composition of the Mg-Zn-Ca system for specific biomedical implant and coating applications considering mechanical strength, degradation rate, and cell viability continues to elude researchers. In addition, Fe-Mg-Zn alloys, which have been called the ‘trifecta of bioresorbable alloys’³⁵, have never been previously tested. Much of this deficiency results from the fact that current processing routes are not efficient for optimizing these new alloys.

The ability to choose the right alloy for a particular bioresorbable implant depends on the following three key properties:

1. *Mechanical*: Hardness, modulus, friction, and wear (especially for orthopedic implants);
2. *Biological*: Degradation rate (tunable depending on use; e.g.: vascular vs. orthopedic, young vs. old patients, etc.), excellent cell viability, and low toxicity;
3. *Manufacturability*: Cheap, alloys easy to produce and form (ideally 3D printable on-site or thermoplastically formable^{36, 37}, potentially also foams and cellular structures^{38, 39}).

Metallic glasses are a material class that lack grain boundaries and as a consequence exhibit a much lower degradation rate. As an example, the degradation of mechanical properties of bones and the healing rates of bones over time with age has been well studied considering orthopedic implant applications^{40, 41}. For such use, it is necessary that the implant takes up most of the mechanical load to facilitate healing during the initial stages and then slowly degrade over time to avoid stress shielding^{42, 43}. It is therefore important to consider the degradation rates (release of metallic ions and degradation of mechanical properties) of bioresorbable implants in the body, which might be significantly different for children, adults, and the elderly. As another example, BMG's as thin film coatings on current biomedical implants based on Ti-alloys or stainless steel

may be ideally suited due to their higher wear resistance, cell adhesion, and improved degradation characteristics when compared to conventional crystalline bioresorbable alloys.

From the discussion above, we see that an experimental approach is missing that is able to rapidly identify good glass formers with suitable chemical composition that are optimized for the intended application with respect to the three key properties listed above. Towards this end, this research employs a high-throughput approach based on creating materials libraries with combinatorial sputtering that are then characterized in a rapid and highly automated fashion. Combinatorial sputtering as a tool for rapid materials discovery and characterization is, of course, not new; however, while it has been widely applied to discover new materials, to identify mechanisms, and to optimize for a plurality of properties^{25, 44-50}, an application to the discovery of bioresorbable materials has not yet been reported. Thereby, we focused on material libraries in the Mg-Zn-Ca/Fe system with composition ranges that have not been previously explored. Out of the above-listed three key property families, this initial paper screens mechanical properties using nanoindentation, which allows us to correlate them with composition and atomic structure. Further studies will then be required to relate the uncovered trends to other important materials characteristics such as degradation rates, electrochemical properties, and cell viability.

2. EXPERIMENTAL SECTION

The combinatorial libraries were produced using a confocal DC magnetron co-sputtering system (AJA International, model ATC 2200), whose general geometric setup is sketched in Fig. 1a. The sputtering guns are arranged tetrahedrally around the substrate, pointing at it at an angle of 29.8° towards the normal axis, which enables the deposition of compositionally graded films by varying either the sputtering power applied on the targets or by changing the target-to-substrate orientation. Sputtering targets of purities 99.95% or better, purchased from Kurt Lesker Company, were used

with exception of the Ca target, which featured a purity of 99.5%. The elastic properties, densities, and melting temperatures of the individual elements Mg, Zn, Ca and Fe are shown in Table 1 in the supplementary section. The substrates were 100 mm diameter, 550 μm thick, single-side polished Si wafers purchased from WRS Materials (San Jose, CA). The substrates were masked with 100 mm diameter and 0.01" thick steel masks that pattern the library into individual circular patches with a diameter of 3 mm each on a square grid with 6 mm center-to-center spacing in order to independently evaluate the mechanical properties. Before sputtering, the processing chamber was evacuated to a base pressure level of less than 5×10^{-7} Torr. The films were then processed in flowing ultra-high purity argon (TechAir Connecticut) at a pressure of 5.8 mTorr. For the Mg-Ca-Zn alloy library, a film with a total thickness of $\approx 1 \mu\text{m}$ was co-sputtered at powers of 89 W, 116 W, and 28 W for Mg, Ca, and Zn, respectively. For the Fe-Mg-Zn alloy library, a film with similar thickness (i.e., $\approx 1 \mu\text{m}$) was co-sputtered, but now at powers of 37 W, 38 W, and 30 W for Mg, Fe, and Zn.

X-Ray diffraction (XRD) was conducted using a Rigaku Smartlab with Cu $K\alpha$ radiation and a 2 mm beam mask. The system was automated yielding an XRD pattern for each library patch. Similarly, an Oxford Instruments X-Max detector attached to a Zeiss Sigma VP field emission scanning electron microscope with an automated method was used to analyze the elemental composition of each patch by energy dispersive X-ray spectroscopy (EDX). Nanoindentation testing was carried out on the combinatorial sputtered wafers using an iNano system (Nanomechanics Inc., Oak Ridge, TN), which allows applying forces up to 50 mN with a resolution of 0.2 nN. A Berkovich tip calibrated on standard fused silica samples for contact area with respect to the indentation depth⁵¹ was used, and experiments were run in the continuous

stiffness measurement mode ^{52, 53} with the peak depth of the indentation set to 100 nm to make sure that results are not (or at least only minimally) affected by substrate effects.

In the 1970's, Bulychev, Alekhin, Ternovskii, Shorshorov and coworkers ⁵⁴⁻⁵⁷ developed an equation to relate the stiffness S (with $S = dP/dh$, where P is the load on sample and h is the displacement into the surface) to the reduced modulus E^* of the material using the load and displacement measured during an indentation test

$$S = \frac{dP}{dh} = 2E^* \frac{\sqrt{A}}{\sqrt{\pi}} \quad , \quad (1)$$

where the reduced modulus or Hertz modulus $E^* = ((1 - \nu_m^2)/E_m + ((1 - \nu_i^2)/E_i)^{-1}$ is obtained from Young's modulus and Poisson's ratio of the sample (E_m , ν_m) and the indenter material ($E_i = 1141$ GPa, $\nu_i = 0.07$ for diamond), respectively. Extending on this approach, Oliver and Pharr demonstrated in 1992 ⁵¹ that Eq. (1), which was originally developed for spherical and cylindrical indenters, is valid for any axisymmetric indenter with an infinitely smooth profile and can therefore be used to determine the elastic properties of a material. While the loading segment in a nanoindentation experiment for a majority of materials is elastic-plastic, the unloading stage is purely elastic. Overall, the method proposed by Oliver and Pharr ⁵¹, which uses the unloading curve to estimate the modulus and hardness of a material, is one of the most widely used methods to calculate elastic properties of a material in most commercial nanoindenters. Since BMGs can be assumed to be elastically isotropic materials, the effective modulus for the material during indentation is given by ⁵⁸⁻⁶⁰

$$E_{\text{Effective}}^m = E_m / (1 - \nu_m^2) \quad . \quad (2)$$

As the amount of pile up or sink-in during indentation is unknown, the Oliver-Pharr hardness, which assumes sink-in behavior, is reported. Tabor⁶¹ observed that when the strain e is ≈ 0.08 , which corresponds to the average plastic strain for a Vickers indenter regardless of the initial state of strain hardening⁶²⁻⁶⁴, the hardness is approximately three times the yield strength σ_y . For non-strain hardening materials, it has been theoretically and experimentally shown that the hardness H is related to the yield/flow stress σ_y by the equation $H \approx 2.9\sigma_y$ ⁶²⁻⁶⁴. Based on Tabor's findings, various researchers have also observed a good correlation between H , σ_y , and the fracture strength for BMGs, respectively^{33, 64}.

3. RESULTS AND DISCUSSION

Figure 1b shows a typical Mg-Zn-Ca materials library fabricated using combinatorial sputtering containing 177 alloy patches of 3 mm diameter each. Due to the geometric setup of the sputtering sources, a thickness variation of less than 20% is observed from center to edge. In addition, the high cooling rates in sputtering allow us to obtain amorphous/glassy structure at compositions that are often not accessible through bulk processing methods. The results of the materials characterization by EDX, XRD, and nanoindentation are shown in Figures 2 and 3 for the Mg-Zn-Ca and the Fe-Mg-Zn alloy library, respectively, and will be discussed in following three sections.

Composition analysis by energy dispersive X-ray spectroscopy

The composition gradient of the Mg-Zn-Ca and the Fe-Mg-Zn alloy library was chosen to include a range of compositions that has not been studied previously. Energy dispersive X-ray spectroscopy (EDX) composition analysis indicates that the Mg-Zn-Ca sputtered wafer (Figure 2a) covers a composition range of $\sim 15 - 85$ at.% Mg, $\sim 5 - 55$ at.% Zn, and $\sim 5 - 60$ at.% Ca, while the Fe-Mg-Zn library (Figure 3a) features a composition range of $\sim 26 - 84$ at.% Mg, $\sim 10 - 61$ at.% Zn, and $\sim 7 - 55$ at.% Fe. In-patch variations, which can arise depending on the patch area, are

found to be minimal. Therefore, the compositions determined at the center of each patch are used for the following analyses.

Structural analysis by X-ray diffraction

Automated X-ray diffraction analysis is used to identify the structure (crystalline vs. amorphous) in the alloy systems following similar procedures as introduced in previously reported research⁴⁷. As mentioned earlier, the Mg-Zn-Ca system has been of interest as a bio-resorbable alloy but not been well studied since most of the alloys in the system have been manufactured using casting or other traditional manufacturing methods. X-ray diffraction analysis data displayed in Figures 2b and 3b reveal that most of the patches on the combinatorial sputtered wafers in both the Mg-Zn-Ca and the Fe-Mg-Zn system show diffusive patterns without any apparent Bragg peaks associated with crystalline structures, which suggests a glassy nature. A representative XRD of one of the rows in each system is shown in Figure S1 in the supplementary section. Generalizing these findings to compositions not explicitly covered in the library, one can expect that the high cooling rate during deposition by combinatorial sputtering ($\sim 10^8$ K/s⁶⁵) will result in a glassy state over an even broader composition range⁶⁶, allowing alloy compositions with marginal glass forming to be used for coating applications as well.

Mechanical property analysis by nanoindentation

Figures 2c/2d and 3c/3d show the results of the nanoindentation testing on the Mg-Zn-Ca and the Fe-Mg-Zn material libraries as function of composition. Thereby, the effective material modulus $E_{\text{Effective}}^m$ and the Oliver-Pharr hardness H are mapped as a function of the at.% composition. To better reveal trends, it is then instructive to plot the yield strength σ_y calculated using Tabor's equation as a function of their composition instead, which is shown in Figures 4a and 4b for the Mg-Zn-Ca and the Fe-Mg-Zn systems, respectively. When presented in this representation, an

obvious dependence of the mechanical properties on the concentration of Zn in the alloys for the Mg-Zn-Ca system can be identified. An increase in H and σ_y coincides with an increase in the Zn content, which has also been reported by other researchers³³ for alloys in the Mg-Zn-Ca system. For alloys in the Fe-Mg-Zn system, an increase in the Zn or the Mg content improves the yield strength up to a certain limit (~ 35 at.% Zn and ~ 50 at.% Mg), after which the mechanical properties deteriorate. Comparing these results with our previously developed guidelines for material selection while considering only mechanical properties, it can be seen that almost the entire bioresorbable alloy library of Mg-Zn-Ca and Fe-Mg-Zn investigated here has the potential to be employed in either vascular or orthopedic applications, replacing the currently used non-resorbable materials (stainless steel and titanium). Note, however, the hardness and the elastic modulus values reported in Figures 2 and 3 do not take the increase in contact area due to pile-up into account, which means that actual values could be significantly lower⁶⁷. It is also important to note that the hardness and modulus measurements of magnetron sputtered thin films can be affected by residual stresses (compressive or tensile) that may arise due to energetic particle bombardment, film/substrate lattice misfits, and deposition parameters (substrate bias, working pressure, etc.) as shown by Chiang et al. for Zr-based ($Zr_{47}Cu_{31}Al_{13}Ni_9$) magnetron sputtered thin films⁶⁸.

Experimental and theoretical modulus comparison

In composite mechanics, an upper and lower bound for the elastic modulus of a material with known volume fraction of its constituents is estimated based on either a uniform stress or a uniform strain assumption⁶⁹. When the stress is uniform, we obtain E from $E = \frac{1}{\sum \frac{x_i}{E_i}}$, which represents the lower bound. If, however, the strain is presumed to be uniform, we obtain an upper bound using $E = \sum x_i E_i$. In both cases, the sum is taken over all constituent elements, x_i is the volume fraction

of the constituent element, and E_i is elastic constant of the corresponding constituent element of the material. Previous researchers⁷⁰⁻⁷² found that when assuming a uniform atomic volume (i.e., using the atomic fraction instead of the volume fraction) in the equation that assumes uniform stress, the ratio of calculated elastic modulus to experimental results was found to be in the range of 0.93 to 1.2 based on results from 21 different BMG systems.

To provide a check on how estimates for the modulus calculated from the uniform stress-based model compare to the experimental results obtained with nanoindentation, the theoretical estimates were plotted in Figure 5 in the same way as the experimental data was plotted in Figures 2c and 3d. Comparing the figures, it can be seen that although the trends are similar, the theoretical values for the Fe-Mg-Zn system are much closer to experimental values obtained, than the theoretical values for the Mg-Zn-Ca system, which are found to be much lower than the experimental values. This discrepancy may be due to the fact that the atomic volumes of the constituent elements are not the same (cf. Table 2 – Supplementary section).

Material selection for implants and coatings

Materials used for implants and coatings on implants must be able to encourage cell attachment (endothelial for vascular^{73, 74}, osteoblasts and osteoclasts for orthopedic⁷⁵⁻⁷⁷), maintain mechanical integrity during the remodeling period (>6-12 months for vascular⁷⁸, >6 months for orthopedic⁷⁹), reduce stress shielding (mechanical compliance)^{15, 23, 35, 41, 78}, and feature appropriate degradation rates so as to reduce hydrogen evolution (<10 $\mu\text{L}\cdot\text{cm}^{-2}\cdot\text{day}$ for both vascular and orthopedic applications^{3, 79}). All of the above parameters vary with physiology, age, gender, and other numerous factors, making the choice of an appropriate material difficult.

For example, if a material needs to *exactly match* the properties of the surrounding tissue in vascular applications, the implant would have to exhibit a yield strength of at least 200 MPa

and a low elastic modulus of <10 GPa, but be stiff enough to maintain the necessary radial strength needed to support the artery or vascular tissue over at least 10^7 fatigue cycles^{3-6, 15}. For orthopedic applications, the yield strength would have to be greater than 230 MPa with a modulus of ≈ 10 -40 GPa, which is meant to approximately equal the mechanical properties of human bones^{7, 13, 40-42}. However, current commonly used materials for implants such as stainless steel- and titanium-based alloys have much higher moduli on the order of ≈ 200 GPa and ≈ 100 GPa, respectively. This is because directly after surgery, a mechanical compliance mismatch is necessary to allow the implant to take up most of the load and let the tissue heal. However, after the tissue has healed and remodeled, this initially favorable property choice presents a drawback as the implant still takes up most of the mechanical load and causes stress shielding. As an example, for an implant or coating application with a requirement of modulus from 50-60 GPa, the Mg-Zn-Ca system studied has ~ 15 different compositions with modulus within that range, however the compositions vary from ~ 25 at. % - ~ 85 at. % Mg. This range of compositions would result in varying biological response (compatibility, cell viability, degradation rate, etc.) with the same starting mechanical compliance, thus allowing researchers to choose the most appropriate composition based on the implant requirements.

Depending on the intended application, the composition space for the Mg-Zn-Ca and the Fe-Mg-Zn alloy systems that are suitable for clinical applications may therefore include a wide range of alloy compositions, starting from those exhibiting mechanical properties that replicate the ones encountered in the surrounding tissue or bones to alloys featuring properties that mirror the ones of titanium alloys and stainless steel. At the same time, alloys with similar mechanical properties may further distinguish by offering a variety of different degradation rates, thereby

enabling surgeons to choose the right composition keeping in mind the various physiological constraints.

4. CONCLUSIONS

In this work, combinatorial sputtering was used to identify alloy compositions of potential interest as bioresorbable implant or coating materials. Mg-Zn-Ca and Fe-Mg-Zn alloy thin film libraries were created with graded compositions and characterized using energy dispersive x-ray spectroscopy, x-ray diffraction, and nanoindentation to scan through the composition, structure, and selected mechanical properties. The data reveal that the Mg-Zn-Ca system shows a strong dependence of hardness on the Zn content. In addition, hardness, effective moduli, and yield strength increase in both systems with an increase in Mg at. % up to a certain point (~40-50 at. %), after which the values reflecting these properties start to decline. Considering just mechanical compliance, most of the alloy compositions analyzed in both the Mg-Zn-Ca and the Fe-Mg-Zn composition space, which are all expected to be bioresorbable, were found to be promising candidate materials to replace existing non-bioresorbable materials like stainless steel and titanium alloys in clinical applications.

More generally, the advent of new processing methods and manufacturing techniques for bulk metallic glasses such as additive manufacturing, thermoplastic forming, and 3D printing opens up new avenues to make alloys such as the ones presented in this research available for clinical applications. This research provides a first step towards establishing a library of bioresorbable materials from which to choose when selecting alloys for artificial implants. Towards this end, the above trends and data for the mechanical properties are to be used in conjunction with other relevant properties such as time dependent degradation of mechanical

properties in simulated body fluids, electrochemical properties, cell viability, etc., to identify alloys best suited for patient- and application-specific purposes.

SUPPORTING INFORMATION

Original data sets for the modulus and hardness measurements are available from the author upon request. All combinatorial data will be publicly available in our online data repository “MAP” (<http://materialsatlasproject.org/>).

ACKNOWLEDGEMENTS

Financial support by the Department of Energy (Grant No. DE-SC0016179) is gratefully acknowledged. The combinatorial synthesis was supported by NSF DMR through award #1609391. In addition, we thank G. M. Pharr for access to the nanoindenter and S. Suib for access to the facilities at the Institute of Materials Science at the University of Connecticut.

CONFLICT OF INTEREST

The authors declare no conflict of interest.

REFERENCES

1. H. Sigel, *Met Ions Biol Syst*, 1985, **19**, R3-R3.
2. X. Gu, Y. Zheng, Y. Cheng and S. Zhong, *Biomaterials*, 2009, **30**, 484-498.
3. P. K. Bowen, E. R. Shearier, S. Zhao, R. J. Guillory, F. Zhao, J. Goldman and J. W. Drelich, *Adv Healthc Mater*, 2016, **5**, 1121-1140.
4. Z. Wang, N. Li, R. Li, Y. Li and L. Ruan, *Progress in Natural Science: Materials International*, 2014, **24**, 423-432.
5. N. T. Kirkland, *Corros Eng Sci Techn*, 2012, **47**, 322-328.
6. P. Smith, *Springerbrief Mater*, 2014, DOI: 10.1007/978-3-319-02123-2_1, 1-12.
7. S. Pal, *Design of Artificial Human Joints & Organs*, 2014.
8. P. Smith, *Springerbrief Mater*, 2014, DOI: 10.1007/978-3-319-02123-2_2, 13-37.
9. N. T. Kirkland, G. Williams and N. Birbilis, *Corros Sci*, 2012, **65**, 5-9.
10. J. Walker, S. Shadanbaz, N. T. Kirkland, E. Stace, T. Woodfield, M. P. Staiger and G. J. Dias, *J Biomed Mater Res B*, 2012, **100b**, 1134-1141.
11. N. T. Kirkland, N. Birbilis and M. P. Staiger, *Acta Biomater*, 2012, **8**, 925-936.
12. G. L. Song and A. Atrens, *Adv Eng Mater*, 1999, **1**, 11-33.
13. Y. F. Zheng, X. N. Gu and F. Witte, *Materials Science and Engineering: R: Reports*, 2014, **77**, 1-34.
14. G. L. Song and A. Atrens, *Adv Eng Mater*, 2003, **5**, 837-858.
15. M. Moravej and D. Mantovani, *Int J Mol Sci*, 2011, **12**, 4250-4270.
16. X.-N. Gu and Y.-F. Zheng, *Frontiers of Materials Science in China*, 2010, **4**, 111-115.
17. M. F. Ashby and A. L. Greer, *Scripta Materialia*, 2006, **54**, 321-326.
18. J. Schroers, G. Kumar, T. M. Hodges, S. Chan and T. R. Kyriakides, *Jom-U.S.*, 2009, **61**, 21-29.
19. G. Kumar, H. X. Tang and J. Schroers, *Nature*, 2009, **457**, 868-872.
20. M. Hasan, J. Schroers and G. Kumar, *Nano Lett*, 2015, **15**, 963-968.
21. J. Padmanabhan, M. J. Augelli, B. Cheung, E. R. Kinser, B. Cleary, P. Kumar, R. H. Wang, A. J. Sawyer, R. Li, U. D. Schwarz, J. Schroers and T. R. Kyriakides, *Sci Rep-Uk*, 2016, **6**.
22. J. Padmanabhan, E. R. Kinser, M. A. Stalter, C. Duncan-Lewis, J. L. Balestrini, A. J. Sawyer, J. Schroers and T. R. Kyriakides, *Acs Nano*, 2014, **8**, 4366-4375.
23. D. C. Hofmann, R. Polit-Casillas, S. N. Roberts, J. P. Borgonia, R. P. Dillon, E. Hilgemann, J. Kolodziejska, L. Montemayor, J. O. Suh, A. Hoff, K. Carpenter, A. Parness, W. L. Johnson, A. Kennett and B. Wilcox, *Sci Rep-Uk*, 2016, **6**.
24. Y. Li, A. D. Taylor, T. Kyriakides and J. Schroers, *in review*, 2014.
25. J. Y. Li, F. S. Gittleston, Y. H. Liu, J. B. Liu, A. M. Loye, L. McMillon-Brown, T. R. Kyriakides, J. Schroers and A. D. Taylor, *Chem Commun*, 2017, **53**, 8288-8291.
26. X. Gu, G. J. Shiflet, F. Q. Guo and S. J. Poon, *J Mater Res*, 2005, **20**, 1935-1938.
27. O. N. Senkov and J. M. Scott, *Journal of Non-Crystalline Solids*, 2005, **351**, 3087-3094.
28. B. Zberg, P. J. Uggowitzer and J. F. Löffler, *Nat Mater*, 2009, **8**, 887-891.
29. M. Ramya, S. G. Sarwat, V. Udhayabanu, S. Subramanian, B. Raj and K. R. Ravi, *Materials & Design*, 2015, **86**, 829-835.
30. W. Jiao, W. Jiao, K. Zhao, D. Q. Zhao and X. K. Xi, *Journal of non-crystalline solids*, 2010, **356**, 1867-1870.
31. H. Li, Y. Zheng and L. Qin, *Progress in Natural Science: Materials International*, 2014, **24**, 414-422.

32. R. Babilas, A. Bajorek, P. Sakiewicz, A. Kania and D. Szyba, *Journal of Non-Crystalline Solids*, 2018, **488**, 69-78.
33. T. B. Matias, V. Roche, R. P. Nogueira, G. H. Asato, C. S. Kiminami, C. Bolfarini, W. J. Botta and A. M. Jorge, *Materials & Design*, 2016, **110**, 188-195.
34. J. Li, F. S. Gittleson, Y. Liu, J. Liu, A. M. Loye, L. McMillon-Brown, T. R. Kyriakides, J. Schroers and A. D. Taylor, *Chem Commun (Camb)*, 2017, **53**, 8288-8291.
35. K. Prasad, O. Bazaka, M. Chua, M. Rochford, L. Fedrick, J. Spoor, R. Symes, M. Tieppo, C. Collins, A. Cao, D. Markwell, K. Ostrikov and K. Bazaka, *Materials*, 2017, **10**.
36. M. A. Gibson, N. M. Mykulowycz, J. Shim, R. Fontana, P. Schmitt, A. Roberts, J. Ketkaew, L. Shao, W. Chen, P. Bordeenithikasem, J. S. Myerberg, R. Fulop, M. D. Verminski, E. M. Sachs, Y. M. Chiang, C. A. Schuh, A. J. Hart and J. Schroers, *Mater Today*, 2018, **21**, 697-702.
37. J. Schroers, *Adv Mater*, 2010, **22**, 1566-1597.
38. B. Sarac, J. Ketkaew, D. O. Popnoe and J. Schroers, *Adv Funct Mater*, 2012, **22**, 3161-3169.
39. Z. Liu, W. Chen, J. Carstensen, J. Ketkaew, R. M. O. Mota, J. K. Guest and J. Schroers, *Acta Mater*, 2016, **105**, 35-43.
40. A. L. Boskey and R. Coleman, *J Dent Res*, 2010, **89**, 1333-1348.
41. E. F. Morgan and M. L. Bouxsein, in *Principles of Bone Biology (Third Edition)*, eds. L. G. Raisz and T. J. Martin, Academic Press, San Diego, 2008, DOI: <https://doi.org/10.1016/B978-0-12-373884-4.00024-0>, pp. 29-51.
42. W. S. Pietrzak, D. Sarver and M. Verstyne, *Bone*, 1996, **19**, 109S-119S.
43. A. R. Amini, J. S. Wallace and S. P. Nukavarapu, *J Long Term Eff Med Implants*, 2011, **21**, 93-122.
44. X. D. Xiang, X. D. Sun, G. Briceno, Y. L. Lou, K. A. Wang, H. Y. Chang, W. G. Wallacefreedman, S. W. Chen and P. G. Schultz, *Science*, 1995, **268**, 1738-1740.
45. J. Cui, Y. S. Chu, O. O. Famodu, Y. Furuya, J. Hattrick-Simpers, R. D. James, A. Ludwig, S. Thienhaus, M. Wuttig, Z. Y. Zhang and I. Takeuchi, *Nature Materials*, 2006, **5**, 286-290.
46. Y. P. Deng, Y. Guan, J. D. Fowkes, S. Q. Wen, F. X. Liu, G. M. Phaff, P. K. Liaw, C. T. Liu and P. D. Rack, *Intermetallics*, 2007, **15**, 1208-1216.
47. S. Ding, Y. Liu, Y. Li, Z. Liu, S. Sohn, F. J. Walker and J. Schroers, *Nat Mater*, 2014, **13**, 494-500.
48. D. Kim, H. C. Shim, T. G. Yun, S. Hyun and S. M. Han, *Extreme Mech Lett*, 2016, **9**, 439-448.
49. S. A. Kube, S. Sohn, D. Uhl, A. Datye, A. Mehta and J. Schroers, *Acta Mater*, 2019, **166**, 677-686.
50. W. Wolf, S. A. Kube, S. Sohn, Y. J. Xie, J. J. Cha, B. E. Scanley, C. S. Kiminami, C. Bolfarini, W. J. Botta and J. Schroers, *Sci Rep-Uk*, 2019, **9**.
51. W. C. Oliver and G. M. Pharr, *J Mater Res*, 1992, **7**, 1564-1583.
52. W. C. Oliver and G. M. Pharr, *J Mater Res*, 2004, **19**, 3-20.
53. W. C. Oliver, *Surfaces and Interfaces in Nanostructured Materials and Trends in Liga, Miniaturization, and Nanoscale Materials*, 2004, 299-299.
54. S. I. Bulychev, V. P. Alekhin, M. K. Shorshorov, A. P. Ternovskii and G. D. Shnyrev, *Ind Lab-Ussr+*, 1975, **41**, 1137-1140.
55. V. P. Alekhin and S. I. Bulychev, *Dokl Akad Nauk Ssr+*, 1978, **238**, 1328-1331.

56. D. A. Kuvaldin, V. P. Alekhin, S. I. Bulychev, S. N. Kaverina and S. I. Altynov, *Russ Metall+*, 1987, 118-121.
57. A. P. Ternovskii, V. P. Alekhin, M. K. Shorshorov, M. M. Khrushchov and V. N. Skvortsov, *Ind Lab-Ussr+*, 1974, **39 (10)**, 1242-1247.
58. J. J. Vlassak and W. D. Nix, *J Mech Phys Solids*, 1994, **42**, 1223-1245.
59. J. J. Vlassak and W. D. Nix, *Philos Mag A*, 1993, **67**, 1045-1056.
60. A. Datye, L. Li, W. Zhang, Y. J. Wei, Y. F. Gao and G. M. Pharr, *J Appl Mech-T Asme*, 2016, **83**.
61. D. Tabor, *British Journal of Applied Physics*, 1956, **7**, 159.
62. H. D. Merchant, G. S. Murty, S. N. Bahadur, L. T. Dwivedi and Y. Mehrotra, *Journal of Materials Science*, 1973, **8**, 437-442.
63. J. R. Cahoon, W. H. Broughton and A. R. Kutzak, *Metallurgical Transactions*, 1971, **2**, 1979-1983.
64. H. S. Chen, J. T. Krause and E. Coleman, *Journal of Non-Crystalline Solids*, 1975, **18**, 157-171.
65. P. Bordeenithikasem, J. B. Liu, S. A. Kube, Y. L. Li, T. X. Ma, B. E. Scanley, C. C. Broadbridge, J. J. Vlassak, J. P. Singer and J. Schroers, *Sci Rep-Uk*, 2017, **7**.
66. Y. H. Liu, T. Fujita, D. P. B. Aji, M. Matsuura and M. W. Chen, *Nat Commun*, 2014, **5**.
67. U. Ramamurty, S. Jana, Y. Kawamura and K. Chattopadhyay, *Acta Mater*, 2005, **53**, 705-717.
68. C. L. Chiang, J. P. Chu, F. X. Liu, P. K. Liaw and R. A. Buchanan, *Appl Phys Lett*, 2006, **88**.
69. Y. Zhang and A. L. Greer, *J Alloy Compd*, 2007, **434**, 2-5.
70. H. B. Yu, X. Shen, Z. Wang, L. Gu, W. H. Wang and H. Y. Bai, *Phys Rev Lett*, 2012, **108**.
71. Z. Zhang, R. J. Wang, L. Xia, B. C. Wei, D. Q. Zhao, M. X. Pan and W. H. Wang, *J Phys-Condens Mat*, 2003, **15**, 4503-4509.
72. B. Zhang, R. J. Wang, D. Q. Zhao, M. X. Pan and W. H. Wang, *Phys Rev B*, 2004, **70**.
73. J. E. Schaffer, E. A. Nauman and L. A. Stanciu, *Acta Biomater*, 2013, **9**, 8574-8584.
74. J. E. Schaffer, E. A. Nauman and L. A. Stanciu, *Metall Mater Trans B*, 2012, **43**, 984-994.
75. K. Anselme, A. Ponche and M. Bigerelle, *P I Mech Eng H*, 2010, **224**, 1487-1507.
76. A. Ponche, M. Bigerelle and K. Anselme, *P I Mech Eng H*, 2010, **224**, 1471-1486.
77. K. Anselme, P. Linez, M. Bigerelle, D. Le Maguer, A. Le Maguer, P. Hardouin, H. F. Hildebrand, A. Iost and J. M. Leroy, *Biomaterials*, 2000, **21**, 1567-1577.
78. H. Hermawan, D. Dube and D. Mantovani, *Woodhead Publ Mater*, 2010, DOI: Doi 10.1533/9781845699246.4.379, 379-404.
79. M. P. Staiger, A. M. Pietak, J. Huadmai and G. Dias, *Biomaterials*, 2006, **27**, 1728-1734.
80. W. Gongyao, L. P. K., S. O. N., M. D. B. and M. M. L., *Adv Eng Mater*, 2009, **11**, 27-34.
81. J. D. Cao, N. T. Kirkland, K. J. Laws, N. Birbilis and M. Ferry, *Acta Biomater*, 2012, **8**, 2375-2383.
82. Q. Zheng, H. Ma, E. Ma and J. Xu, *Scripta Materialia*, 2006, **55**, 541-544.

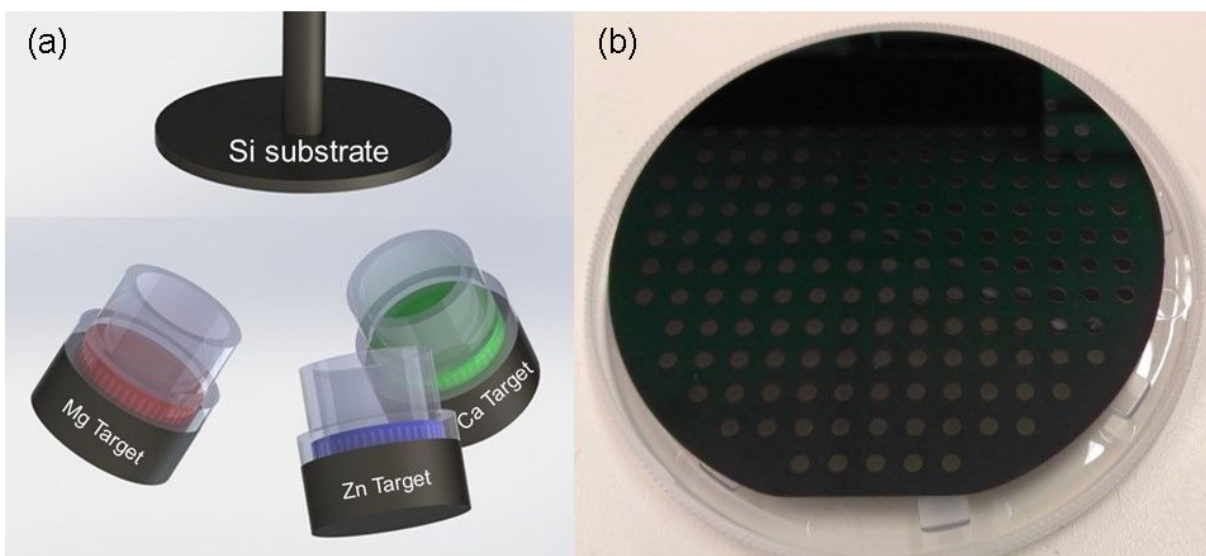
FIGURES

Figure 1: (a) Schematic illustration of the combinatorial sputtering setup; (b) photo of a fabricated Mg-Zn-Ca alloy library.

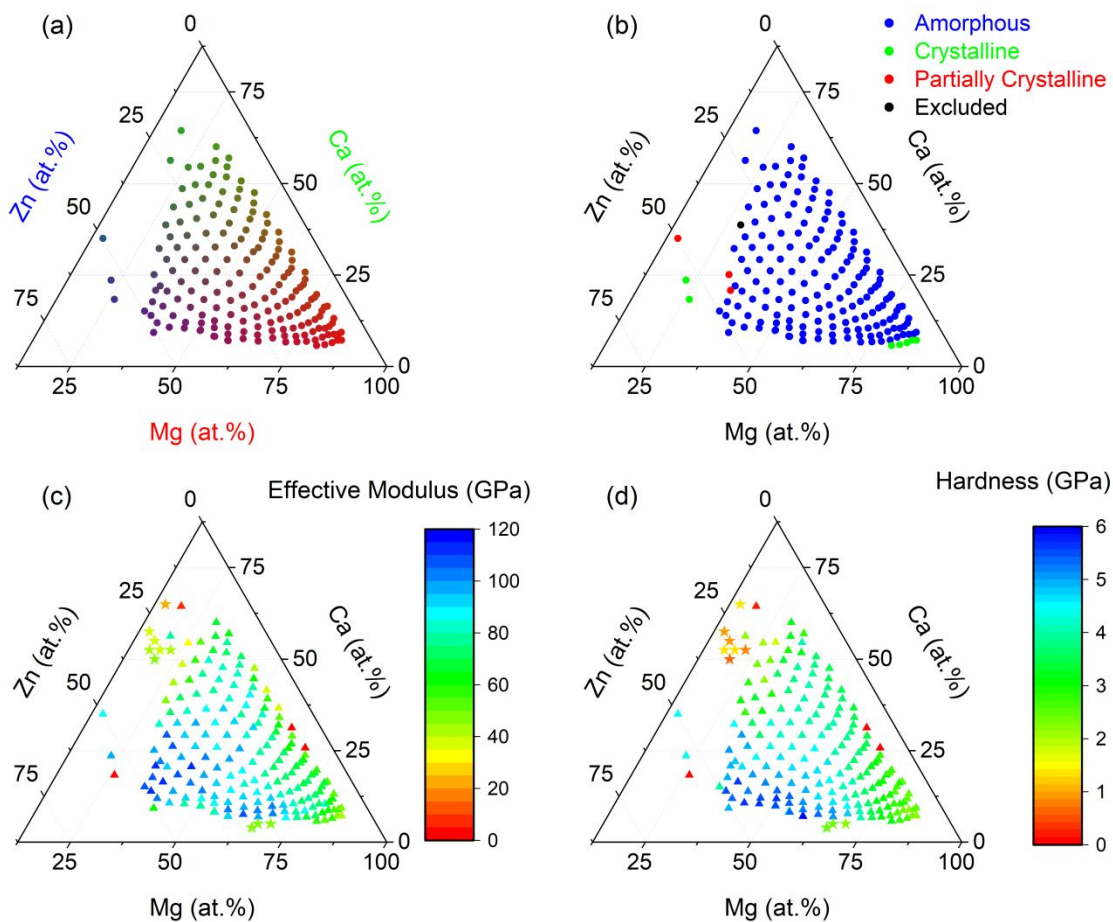


Figure 2: Mg-Zn-Ca alloy library. (a) EDX compositional analysis; (b) XRD analysis; and (c) and (d) effective material modulus $E_{\text{Effective}}^m$ and hardness H (Oliver-Pharr), respectively, obtained by nanoindentation using a Berkovich tip. In both panels (c) and (d), data measured in this work is marked by triangles (\blacktriangle), while stars (\star) indicate modulus and Vickers hardness data taken from previous research (cf. Table 1), which is plotted for comparison. In this context, note in particular that modulus data represented by stars (\star) is calculated using various methods.

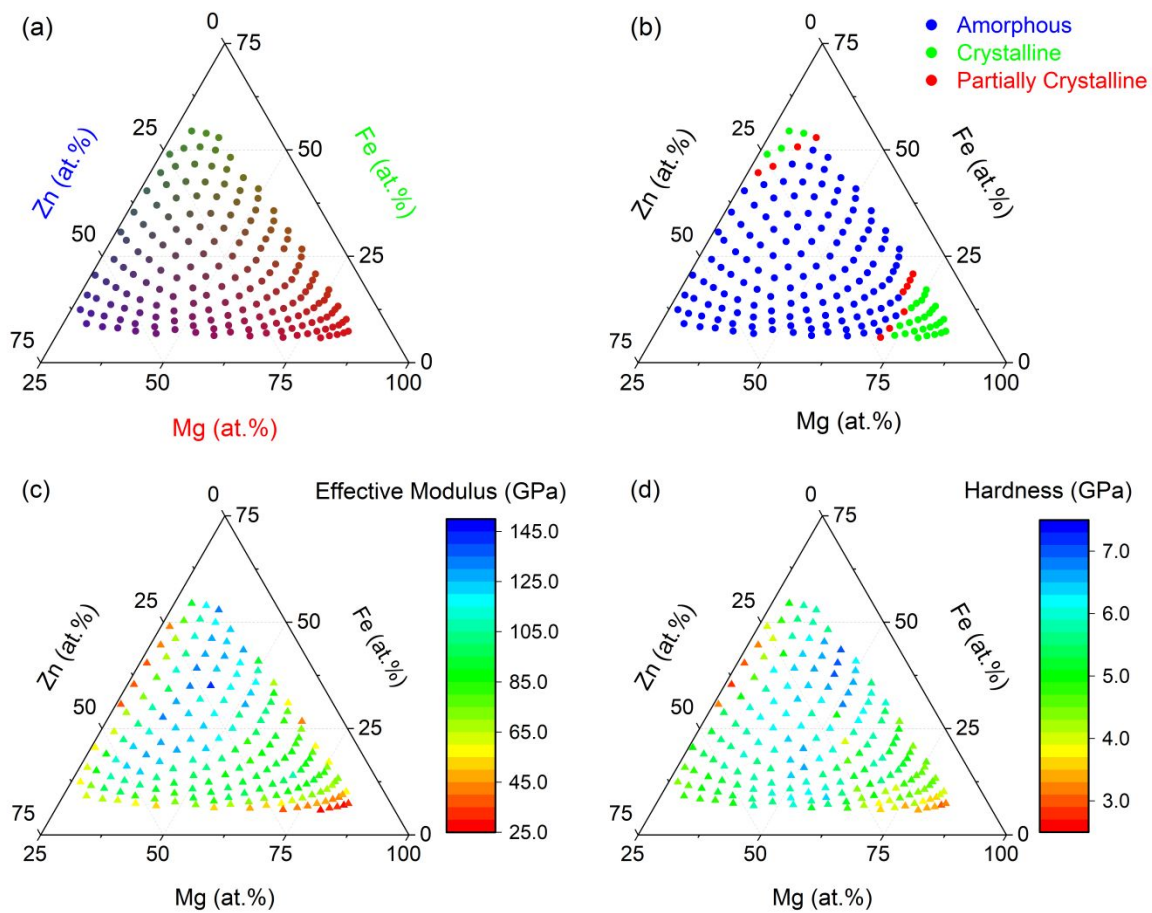


Figure 3: Graphs analogous to the ones in Fig. 2, but now representing the Fe-Mg-Zn alloy library. (a) EDX compositional analysis; (b) XRD analysis; and (c) and (d) effective material modulus $E_{\text{Effective}}^m$ and Oliver-Pharr hardness H obtained by nanoindentation using a Berkovich tip.

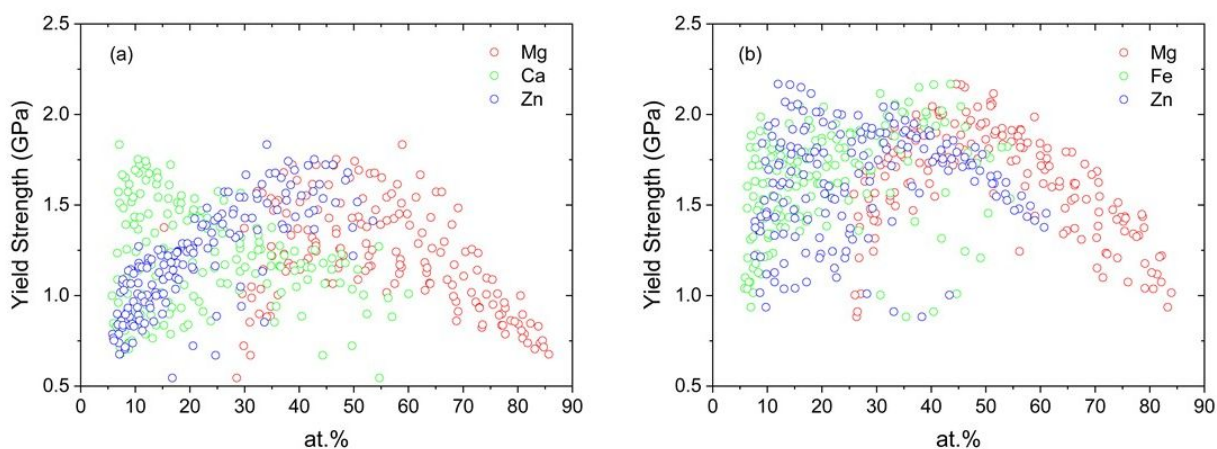


Figure 4: Yield strength σ_y of the different compositions in the (a) Mg-Zn-Ca and (b) Fe-Mg-Zn alloy system, respectively, calculated from the hardness values reported in Figures 2 and 3 using Tabor's relation.

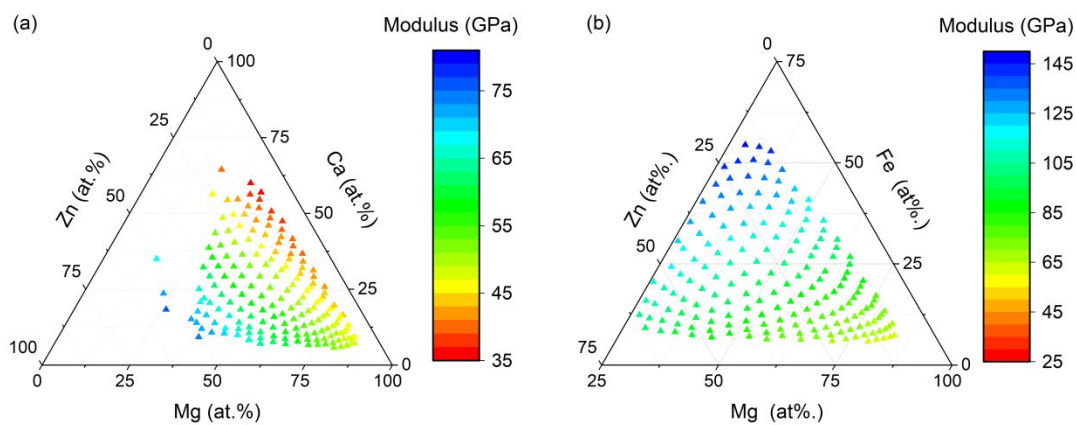


Figure 5: Theoretical modulus calculations based on rule of mixtures for compositions in the (a) Mg-Zn-Ca and (b) Fe-Mg-Zn alloy libraries.

TABLES

Table 1: Mechanical properties of some previously studied Mg-Zn-Ca BMGs.

Mg	Ca	Zn	Young's Modulus (E)	Vickers Hardness (H_V)	Reference
[at.%]	[at.%]	[at.%]	[GPa]	[GPa]	
15	65	20	20	1.42	80
15	57.5	27.5	36.5	0.9	81
17.5	52.5	30	44	1.4	
17.5	55	27.5	36	0.9	
20	50	30	46	0.7	
20	52.5	27.5	39	1.4	
22.5	52.5	25	43	0.8	
70	5	25	47.6	2.16	26, 82
60	6	34	-	2.96	33
73	4	23	-	2.12	